ACS MATERIALS LETTERS

www.acsmaterialsletters.org

Flash Nitrogen-Doped Graphene for High-Rate Supercapacitors

Sheng Zhu,* Fei Zhang, Hai-Gang Lu, Jian Sheng, Lina Wang, Si-Dian Li,* Gaoyi Han,* and Yan Li*

Cite This: *ACS Materials Lett.* 2022, 4, 1863−1871

Read Online

ACCESS | Metrics & More | Article Recommendations | Supporting Information

ABSTRACT: **Novel structured graphene produced by an environmentally-friendly and high-yielding method together with excellent electrochemical energy storage performance is pursued. A one-pot, solvent- and catalyst-free flash Joule heating approach is developed for synthesizing nitrogen-doped graphene and so named as flash nitrogen-doped graphene (FNG). The precursors of amorphous carbon black and urea are quickly converted into high-quality FNG in less than 1 s under a short electrical pulse with a bright flash of blackbody radiation. The prepared FNG product features high graphitization with a turbostratic structure. It delivers a high surface-area-normalized capacitance of 152.8 μF cm^{-2} at 1 A g^{-1}, an extraordinary rate capability with prominent capacitance retention of 86.1% even at 128 A g^{-1}, and a knockdown relaxation time of 30.2 ms. Besides, the assembled symmetric quasi-solid-state supercapacitor exhibits a high energy density of 16.9 Wh kg^{-1} and a maximum power density of 16.0 kW kg^{-1}, as well as desirable cyclic stability (91.2% of initial capacitance is maintained after 10000 cycles). These outstanding performances show that FNG is a promising candidate for exploiting high-performance supercapacitors.**

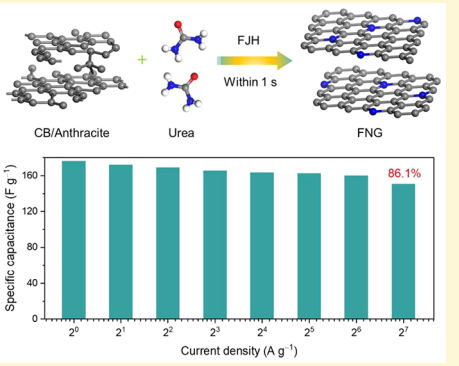

As complementary energy storage devices for rechargeable batteries, supercapacitors (SCs) have gained extensive attention in the past few decades because of their excellent safety, high power density, and outstanding durability.[1−3] The previous research studies have mainly focused on the development of electrode materials by composition modulation and structure optimization, as well as the understanding of the charge storage mechanism.[4−7] Despite tremendous advances in this field, the improvement of energy storage performance with desirable charge capability even at high current densities and scan rates is still a long-standing challenge for practical SCs.[8−10] Currently, the majority of SCs are operated at a charging speed of 0.1−20 A g^{-1} or 2−100 mV s^{-1}, meaning that the charging time ranges from tens of seconds to an hour.[11−14] Further elevating the charging speed can shorten the charging time to meet the demands of high-rate SCs, however, which always induces a deteriorated electrode structure and decayed rate performance.

Compared with pseudocapacitive materials which store energy via surface redox reactions, carbon-based materials have the advantage in deploying high-rate SCs for fast and reversible ion adsorption/desorption at the electrode/electrolyte interface.[15−17] Graphene, with a unique two-dimensional nanostructure, high electrical conductivity, large theoretical surface area, and excellent mechanical flexibility, has been considered as one of the most promising electrode materials.[18−20] SCs based on graphene electrodes synthesized by different methods including liquid chemical oxidation,[21] mechanical exfoliation,[22] chemical vapor deposition (CVD),[23] and arc-discharge[24] have been developed with specific capacitances in the range of 10−200 F g^{-1} in aqueous electrolyte.[25,26] Among these synthetic methods, liquid chemical oxidation and exfoliation are likely to produce a high yield graphene while inevitably undermining the structural integrity.[27,28] Thus, the resultant SCs present an unsatisfactory overall performance, especially an inferior rate performance and power delivery. CVD and arc-discharge favor preparing high-quality graphene that is eminently suitable for fundamental research.[29,30] However, from the industrial perspective, the mass production of graphene is presently limited by several deficiencies such as low production yield, special gaseous conditions, tedious processing techniques, and high cost.

As a powerful electrothermal synthesis technique, the flash Joule heating (FJH) method has recently been utilized for

Received: July 9, 2022
Revised: August 25, 2022
Accepted: August 26, 2022

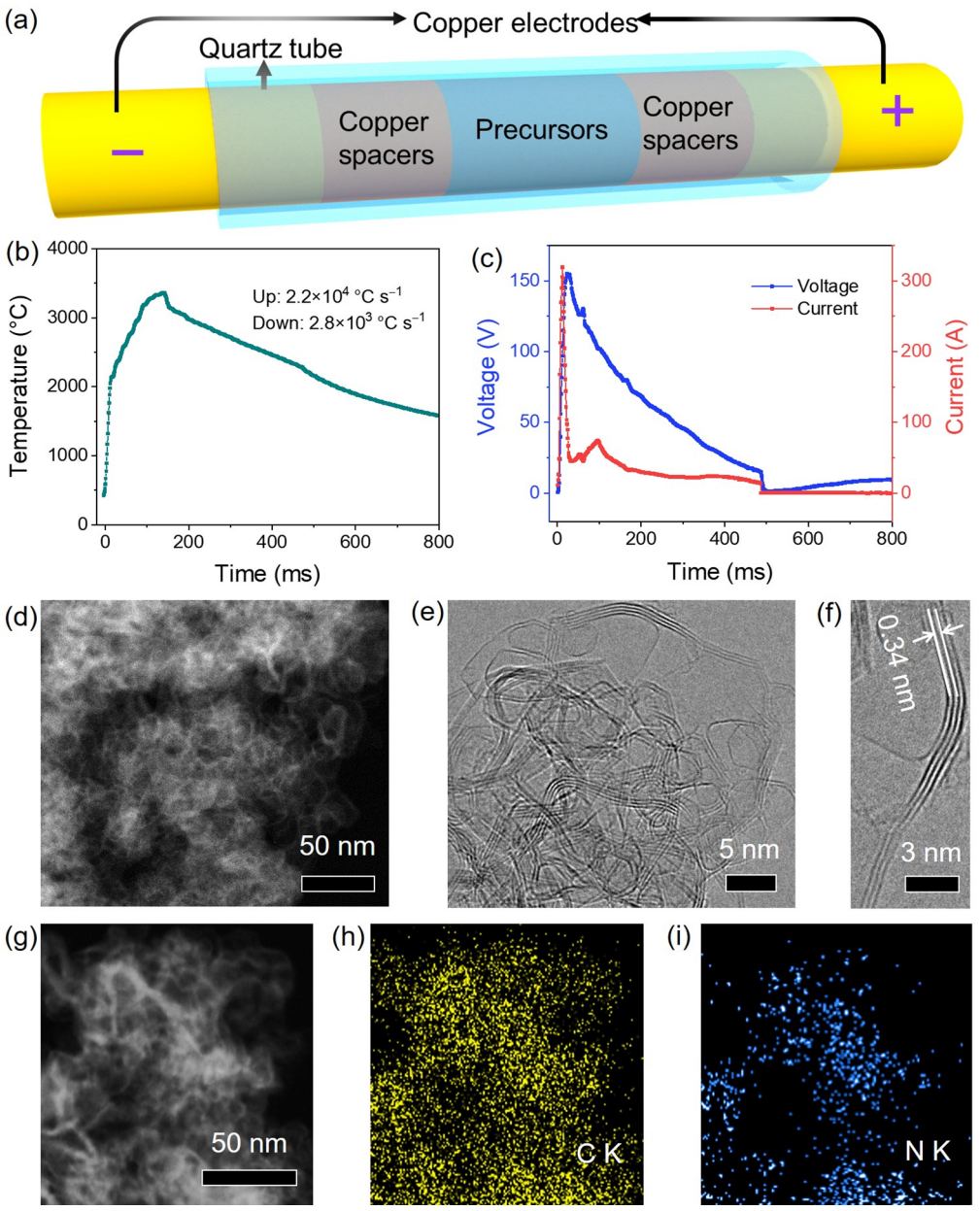

Figure 1. (a) Schematic illustration of a typical flash Joule heating (FJH) reaction device. (b) The real-time temperature during the first FJH synthesis of FNG. (c) The real-time voltage and current during the second FJH synthesis of FNG. STEM image (d), high-resolution TEM images (e, f), and elemental mapping images (g–i) of FNG.

producing high-quality carbon materials with bulk quantities. In 2020, the Tour group[31] first reported the ultrafast gram-scale conversion of any carbon source to flash graphene (FG) by using such an approach. FG features turbostratic morphology with a rotational mismatch between neighboring sheets, leading to similar spectroscopic signatures to high-quality monolayer graphene.[32,33] Beyond the currently used methods, the FJH technique possesses many advantages such as high production yield, simple operation, and high quality of the graphene product. The prepared FG has huge potential in developing high-rate SCs with desirable overall performance.

Inspired by the above analyses, here, we report a one-pot flash Joule heating (FJH) method for efficient synthesis of flash nitrogen-doped graphene (FNG) within 1 s. This process is free of any solvents, catalysts, or reactive gases. The solid precursors endure an ultrahigh temperature (>3000 K) and then a rapid cooling (>10^4 K s^{-1}) to room temperature. During this process, the short electrical pulse with a bright flash of blackbody radiation leads to the ultrafast conversion of amorphous carbon black into graphitized graphene, which is doped by nitrogen. The resultant FNG shows high quality and crystallization with minimal structural defects. As electrode material for supercapacitors, it demonstrates prominent electrochemical performance in terms of high rate capability, low relaxation time, and long-term electrochemical stability.

Results and Discussion. Figure 1a depicts the schematic diagram of a typical FJH reactor which contains a quartz tube, two copper spacers, and electrodes. The optical photos of the FJH system are provided in Figures S1 and S2. To synthesize FNG, carbon black and urea were employed as carbon and nitrogen sources, respectively. The precursors were evenly mixed and enclosed within the quartz tube, followed by

https://doi.org/10.1021/acsmaterialslett.2c00616
ACS Materials Lett. 2022, 4, 1863−1871

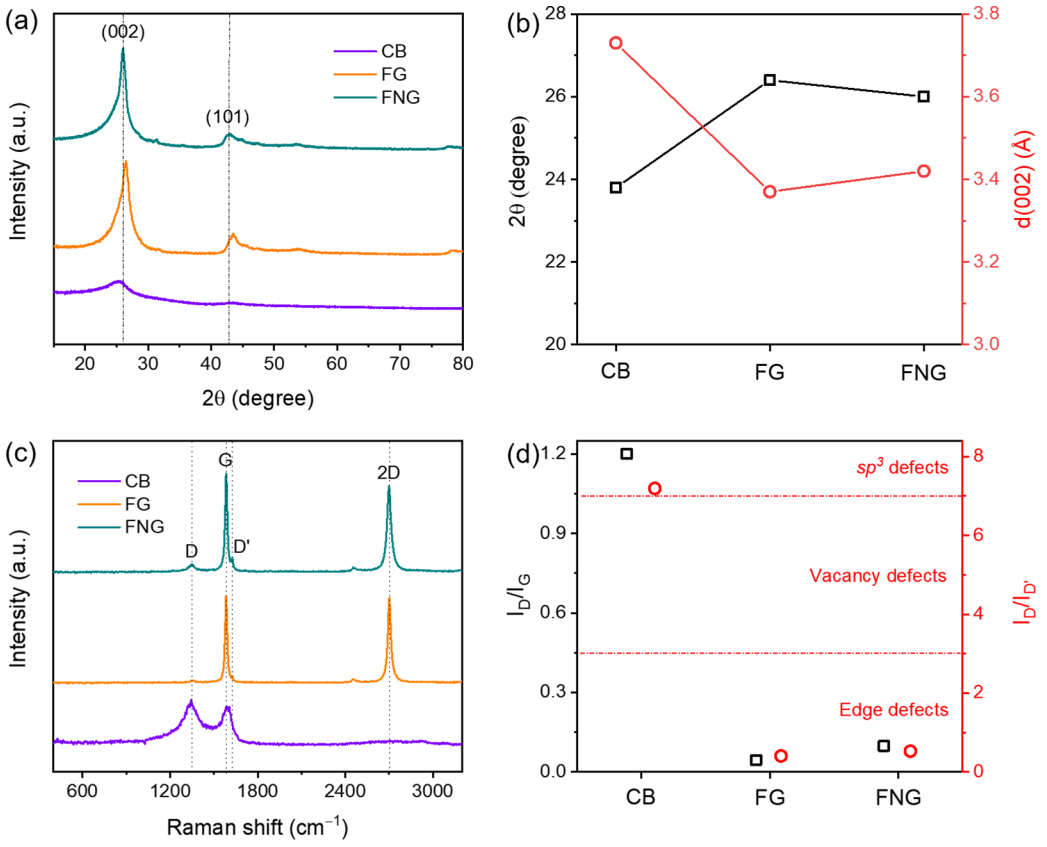

Figure 2. (a) XRD profiles of CB, FG, and FNG. (b) Comparison of 2θ deg and (002) distances of CB, FG, and FNG. (c) Raman spectra of CB, FG, and FNG. (d) Comparison of I_D/I_G and $I_D/I_{D'}$ values of CB, FG, and FNG.

compression between two copper spacers to ensure their complete contact. The electrical conductivity of the precursors can be controlled by varying the distance between two spacers. In this study, the distance was kept as ∼8.5 mm to achieve a small initial resistance within 1 Ω. In order to improve the conversion efficiency from precursors to FNG, twice flashing was performed by transposing the cathode and anode. The detailed experimental parameters of FJH reaction from CB to FNG can be found in Table S1. The real-time temperature, voltage, and current were recorded and shown in Figure 1b,c and Figure S3. During the reactions, the electrodes were connected to a capacitor bank and charged to a voltage of 180 V. The discharge of the capacitor bank leads to superfast heating of precursors to above 3000 °C within 200 ms, and then it cools to room temperature within seconds. The electrical conductivity of the FNG after twice FJH is greatly improved and confirmed by the much higher peak current in Figure S3b. As shown in Figure S4, the sample resistance decreased from 0.62 Ω to 0.34 Ω after FJH reactions. The CB as starting material is predominantly composed of amorphous carbon particles with small graphitic domains. The fast FJH facilitates its efficient conversion to high-value turbostratic N-doped graphene with a high graphitization degree and larger interlayer spacings, which is easier to exfoliate than an AB-stacked structure. As we can see from Figure S5, the FJH process is free of any solvents, catalysts, and reactive gases, having great superiorities compared with the conventional synthetic methods.

As shown in Figure S6, the primary CB powders are comprised of nanospheres with an average diameter of 20−30 nm. After the FJH reaction, the color of the prepared FNG changes from black to gray (Figure S7a). Unlike flat and thin nanosheets that are always found for exfoliated graphene, the scanning electron microscopy (SEM) and transmission electron microscopy (TEM) images of FNG in Figure S7 and Figure 1d present clusters of crumpled nanoflakes with a smooth surface, and these clusters have a uniform size of tens of nanometers. There are no obvious differences on micromorphology between FG and FNG products (Figure S8). It is worth mentioning that we can also obtain FG from cost-effective anthracite, as exhibited in Figure S9. High-resolution TEM images (Figure 1e,f) of the FNG sample exhibit a group of distinctive lattice fringes, confirming the high graphitization degree. FNG features bend/wrinkled morphology and typically has a thickness of 2−6 layers. The interatomic spacing is determined as ∼0.34 nm, corresponding to the turbostratic structure of the FNG material.[32] These findings are also evident by atomic force microscopy images (Figure S10) in which a well-dispersed FNG sheet has a height of ca. 1.7 nm, equal to the thickness of five graphene layers. The uniform distribution of C and N elements is found in the selected area for the FNG sample (Figure 1g−i), indicating the success of N within the graphene framework. Figure S11 shows the nitrogen adsorption−desorption curves of CB and FNG. FNG has a specific surface area of 114.6 $m^2\ g^{-1}$, and this value is lower than that of the CB (290.4 $m^2\ g^{-1}$). During the conversion process, many electrochemical-inactive micropores of amorphous CB were eliminated, resulting in the formation of graphitic FNG with greatly reduced structural defects.

The X-ray diffraction (XRD) profiles of CB, FG, and FNG are supplied in Figure 2a. A broad (002) band located at around 25.5 degree is observed for CB, indicating its low

https://doi.org/10.1021/acsmaterialslett.2c00616
ACS Materials Lett. 2022, 4, 1863−1871

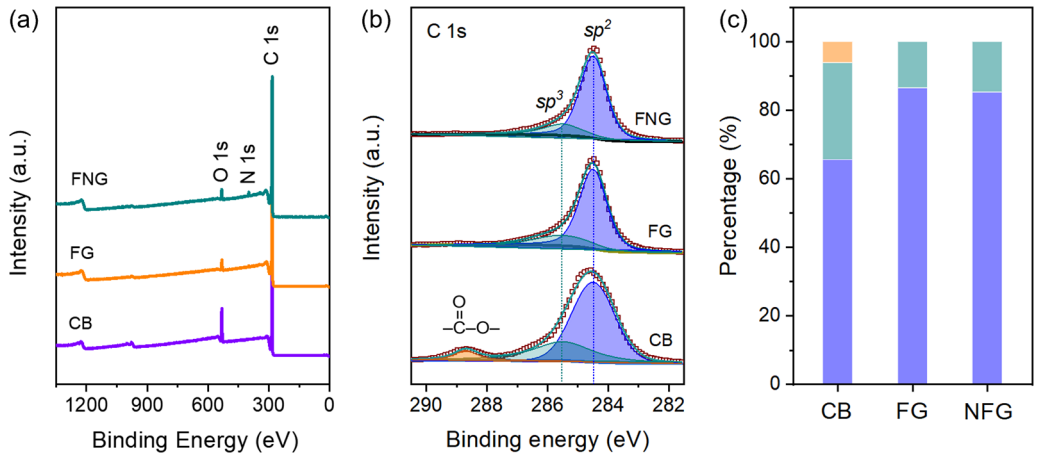

Figure 3. XPS full spectra (a), high-resolution C 1s spectra (b), and percentages of carboxyl (orange), sp^3 (green), and sp^2 (blue) carbon (c) of CB, FG, and FNG.

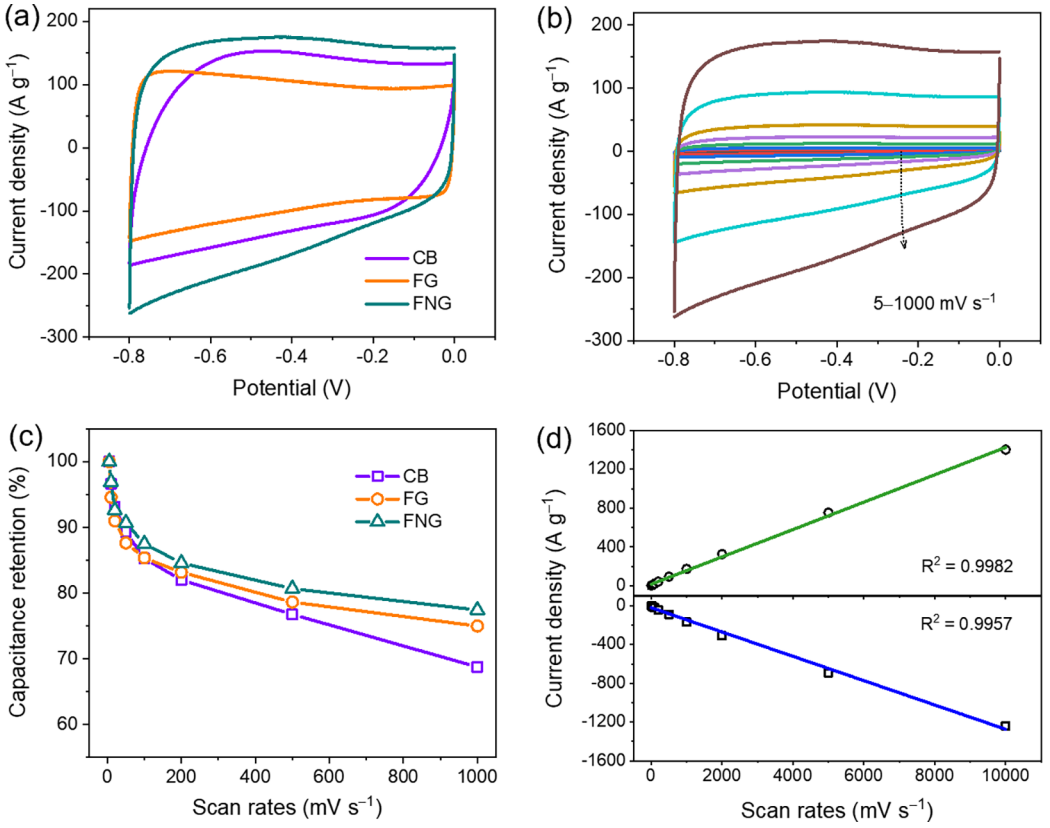

Figure 4. (a) CV curves of CB, FG, and FNG electrodes at a scan rate of 1000 mV s^{-1}. (b) CV curves of the FNG electrode at different scan rates ranging from 5 to 1000 mV s^{-1}. (c) Capacitance retention of CB, FG, and FNG electrodes at increasing scan rates from 5−1000 mV s^{-1}. (d) Plots of charge and discharge current densities versus scan rates from 5 to 10000 mV s^{-1} of the FNG electrode.

graphitization degree. However, FG displays a sharp (002) peak along with a weak (100) peak, which are characteristic signals of turbostratic graphene, confirming the absence of ordered AB-stacking of basal planes.[34,35] After nitrogen doping, the graphitic turbostratic structure was preserved with a downshift of the (002) peak to ~26.0 deg. This result suggests the expansion of interlayer spacing of FNG, which may stem from the heteroatom doping.[36] Figure 2b compares the 2θ deg and interplanar spacing of (002) distances for these samples. Graphitic FNG with high electrical conductivity and a intermediate spacing of 3.42 Å is easier for exfoliation, thus having great potential for high-performance charge storage.

A representative Raman spectrum of the CB is shown in Figure 2c, from which we can observe the high D band (breathing mode of sp^2-carbon atoms in rings) at ~1345 cm^{-1} and G band (bonds stretching of all pairs of sp^2-carbon atoms in rings) at ~1585 cm^{-1}.[35] For FG, it exhibits a very sharp G peak and 2D peak (second-order zone boundary phonons in graphene) at ~2700 cm^{-1}. Their intensity ratio (I_{2D}/I_G) is close to 1, indicating the high graphitization and few layers of the graphene sheets.[37] From the Raman spectra of FG and

https://doi.org/10.1021/acsmaterialslett.2c00616
ACS Materials Lett. 2022, 4, 1863−1871

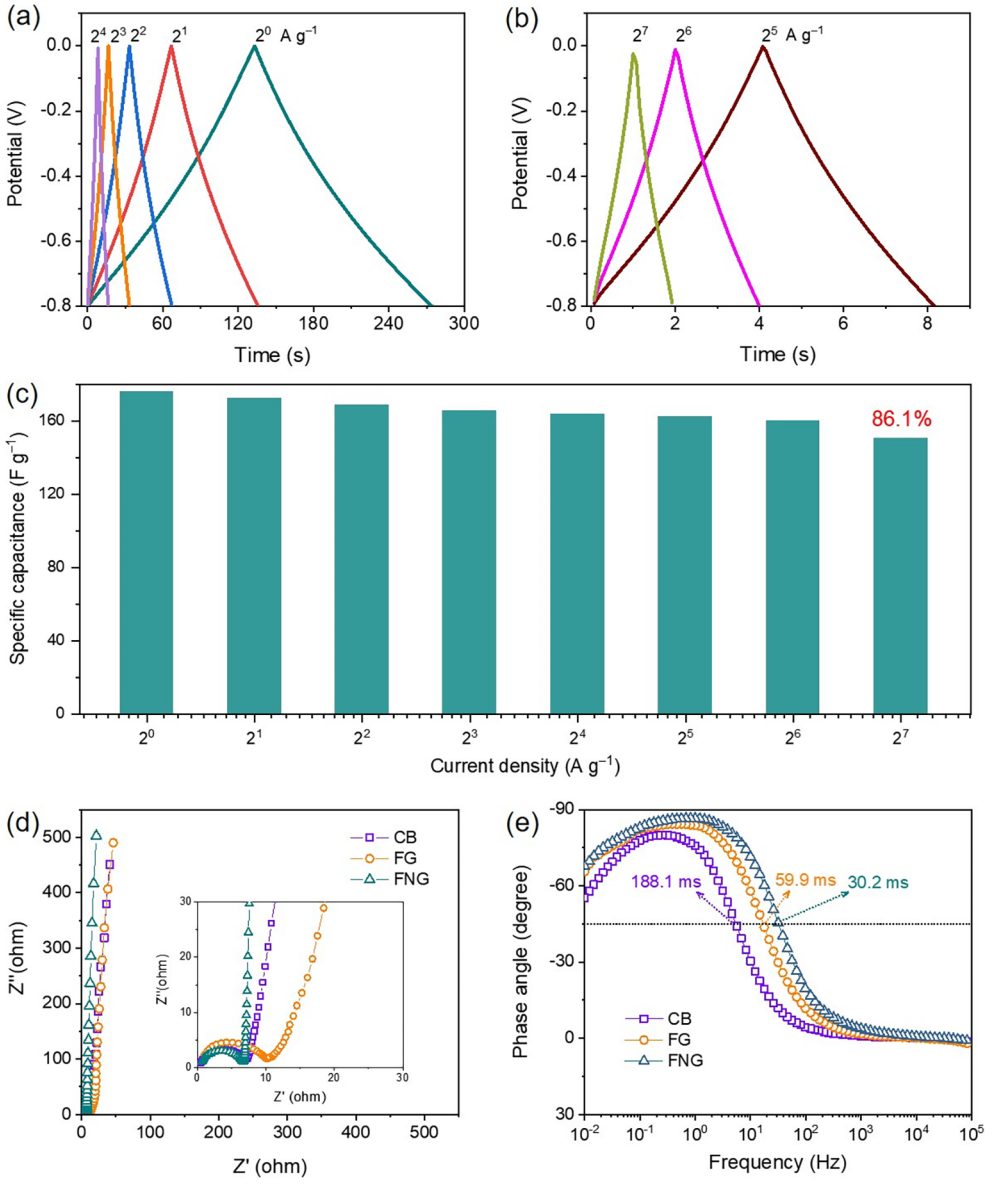

Figure 5. (a) GCD curves of the FNG electrode under different current densities from 2^0 to 2^4 A g^{-1}. (b) GCD curves of the FNG electrode under high current densities of 2^5, 2^6, and 2^7 A g^{-1}. (c) Specific capacitances of the FNG electrode under increasing current densities from 2^0 to 2^7 A g^{-1}. EIS (d) and Bode (e) plots of the CB, FG, and FNG electrodes. The inset in (d) shows enlargement of the EIS plots in high-frequency region.

FNG, we can see another defect-induced D′ peak at ∼1620 cm^{-1}, which stems from the intravalley double resonance process.[38] The intensity ratio of the D and D′ band ($I_D/I_{D'}$) can be used to unveil the defect nature in the atomic structure of graphene.[39] As displayed in Figure 2d, the $I_D/I_{D'}$ values of both FG and FNG are lower than 3, indicative of the location of some structural defects or disorders on the edge sites, rather than the basal plane. The D′ band tends to merge into the G band at a high defect concentration as suggested by Casiraghi.[39] The pristine G band of CB was deconvoluted into two subpeaks containing the D′ band, its $I_D/I_{D'}$ value is higher than 7, confirming the predominant presence of sp^3 defects (Figure S12). These conclusions have been also supported by analyzing the intensity ratios of D and G bands (I_D/I_G). The I_D/I_G value of CB was calculated to be ∼1.2, which is much higher than that of FG and FNG, suggesting the elimination of many structural defects or disorders by the FJH method. Note that FNG shows slightly higher values of both $I_D/I_{D'}$ and I_D/I_G than FG, which can be ascribed to the N-doped substitutional defect sites. The low I_D/I_G and high I_{2D}/I_G values suggest the high quality of the as-prepared graphene, and the comparison with reported graphene materials is provided in Table S2. Note that another possible reason for the low I_D/I_G value is the relative low N content (0.66 wt %) based on the elemental analysis test. Additionally, the distinct TS1 and TS2 peaks in high-resolution Raman spectra (Figure S13) confirm the turbostratic feature of prepared FG and FNG.[32]

Nitrogen doping was also verified by X-ray photoelectron spectroscopy (XPS). From Figure 3a and Figure S14, we observe the N 1s signal for the FNG sample (N ratio: 0.86 at. %). It is mainly deconvoluted into two peaks centered at 400.1 eV (pyrrolic N) and 398.8 eV (pyridinic N). These N species are located at the edge of graphene nanosheets, and they can improve the ion adsorption capability and contribute

https://doi.org/10.1021/acsmaterialslett.2c00616
ACS Materials Lett. 2022, 4, 1863−1871

pseudocapacitance for the FNG sample.[24] The C 1s spectrum (Figure 3b) of CB has been fitted with three components located at 288.7, 285.5, and 284.5 eV, which refer to the surface carboxyl group, sp^3 and sp^2 bonded carbon, respectively.[40,41] After the FJH reaction, the signal at 288.7 eV disappears for both FG and FNG samples accompanied by the intensity decrease of the sp^3 band. As depicted in Figure 3c, the sp^2 contribution of FG is 86.5%, much higher than that of CB (65.6%), confirming the conversion from amorphous carbon to graphitic graphene.

The electrochemical performance of the prepared FNG electrode has been studied in a 6.0 mol L^{-1} KOH electrolyte with a three-electrode configuration. As displayed in Figure 4a, the cyclic voltammetry (CV) curve of FG features a nearly rectangular shape without redox peaks, revealing a typical electrical double-layer capacititance (EDLC) behavior of the highly graphitic carbonaceous materials. Once nitrogen atoms are introduced into the FG, the CV curve of FNG shows two aspects of divergences. First, the total amount of adsorbed charges is remarkably increased as the CV integrated area of FNG is larger than that of FG. Also, distinctive humps in a potential range of −0.6 to −0.3 V suggest a combination of EDLC and pseudocapacitive energy storage behaviors of FNG. Second, the FNG electrode exhibits more fast electrochemical responses at the beginning of both charge and discharge processes, implying the elevated electrical conductivity and unrestrained ion transport. This could be ascribed to the unique graphitic turbostratic structure as well as the favorable interfacial interaction between electrode and electrolyte since the N-doping can improve the surface hydrophilic property of crystalline graphene.[42,43] When scan rates are increased from 5 to 1000 mV s^{-1}, the CV shapes of FNG are well kept (Figure 4b). As we can see from Figure 4c, FNG achieves a capacitance retention of 77.4%, higher than CB (68.8%) and FG (75.0%), confirming the excellent rate performance of FNG. More interestingly, the FNG electrode still demonstrates ideal CV curves at the high scan rate of 2, 5, and 10 V s^{-1} (Figure S17), where no polarization is found in the given potential window, and both the charge and discharge current densities have a desirable linear relationship with the scan rates ranging from 5 to 10000 mV s^{-1} (Figure 4d).

The galvanostatic charge and discharge (GCD) curves of FNG, CB, and FG are provided in Figure 5a,b, Figures S18 and S19. With the current density increases from 1 A g^{-1} to 128 A g^{-1}, the curves of FNG electrode still maintain a nearly ideal triangular shape. It also shows a small IR drop of 0.0015 V at the current density of 1 A g^{-1} and 0.026 V even at 128 A g^{-1} (Figure S20), revealing the robust electrochemical kinetics. In comparison, the higher IR drops are observed for CB (0.0022 V) and FG (0.0036 V) at 1 A g^{-1} (Figure S21); the high value of FG may be attributed to the hydrophobic property. Despite of a low specific surface area, it is worth mentioning that FNG delivers a specific capacitance of 175.1 F g^{-1} at 1 A g^{-1}, outperforming the CB (161.4 F g^{-1}) and FG (126.2 F g^{-1}) electrodes (Figure S22). Its surface-area-normalized capacitance reaches 152.8 μF cm^{-2}; this value surpasses many reported results of diverse carbon materials (Table S3), revealing the prominent ion adsorption capability of the FNG electrode. With an increase in the current densities, the calculated specific capacitances of FNG are 172.2, 168.8, 165.5, 163.6, 162.5, 160.0, and 150.7 F g^{-1} at 2, 4, 8, 16, 32, 64, and 128 A g^{-1}, respectively. A ultrahigh capacitance retention of 86.1% has been thus achieved when the current density changes from 1 A g^{-1} to 128 A g^{-1} (Figure 5c). Such an excellent rate performance is superior to CB and FG, and hardly reported in the literature.

The electrochemical impedance spectroscopy (EIS) technique was conducted with a frequency range from 100 kHz to 0.01 Hz to study the kinetic characteristics of each material. It can be seen from Figure 5d that all of the electrodes show a near-vertical curve in the low-frequency region and a semicircle in the high-frequency region, indicating the ideal capacitor behavior. The highest straight slope of FNG reveals its lowest Warburg resistance (Z_w), and the diameter of the material is related to the charge transfer resistance (R_{CT})).[44,45] The equivalent circuit is provided in Figure S23. As depicted in Figure S24, the FNG electrode affords a smaller R_{CT} of 5.8 Ω compared to the CB (7.6 Ω) and FG (9.5 Ω) electrodes, suggesting that the outer surface of graphene flakes is fully accessed by the electrolyte solution.[46,47] The lower R_{CT} of CB than FG benefits from the surface oxygen-containing groups, and the desirable hydrophilicity facilitates the transfer of electrolyte ions to the electrode and lowering the electrode/electrolyte interfacial resistance. Figure 5e supplies the Bode plots of different electrodes, and their phase angles are lower than −80° at the frequency range of 0.1−10 Hz, approaching the behavior of an ideal capacitor (defined by a phase angle of −90°).[48] The relaxation time constant (τ_0) could be obtained using the equation of $\tau_0 = 1/f_0$ (where f_0 is the frequency at −45°).[49,50] The τ_0 values of the FNG, CB, and FG electrodes are calculated to be 30.2, 188.1, and 59.9 ms, respectively. The low τ_0 of FNG reflects its fast response owing to the enhanced conductivity, stemming from both high graphitization and surface nitrogen doping. Its superior capacitive performances regarding low IR drop, R_{CT}, and τ_0, high normalized capacitance and capacitance retention, are illustrated using Radar plots in Figure 6 and Table S4.

To evaluate the electrochemical energy storage performance of the FNG electrode toward application, symmetric quasi-solid-state SCs were assembled according to the diagram in Figure S25a. Figure S25b displays the CV curves of FNG-based SC at the scan rates of 0.2, 0.5, 1, 2, 5, and 10 V s^{-1}, and

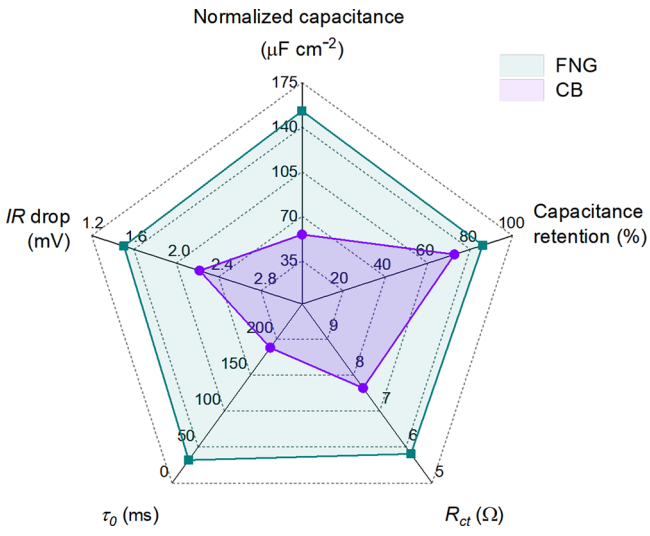

Figure 6. Radar plots of FNG and CB electrodes involving area-normalized capacitance (μF cm^{-2}) at 1 A g^{-1}, capacitance retention (%) at 128 A g^{-1}, R_{CT} (Ω), τ_0 (ms), and IR drop (mV) at 1 A g^{-1}.

https://doi.org/10.1021/acsmaterialslett.2c00616
ACS Materials Lett. 2022, 4, 1863−1871

all of them present a rectangular-like shape in the potential range of 0−1 V. According to the GCD curves in Figure S25c, the specific capacitance of FNG-based SC was calculated to be 121.7 F g^{-1} (73.0 mF cm^{-2}), higher than that of CB-based SC (95.2 F g^{-1}, 57.1 mF cm^{-2}), as compared in Figure S25d. The Ragone plots of two kinds of quasi-solid-state SCs are provided in Figure S26; maximum energy and power densities of 16.9 Wh kg^{-1} and 16.0 kW kg^{-1} were achieved for the FNG-based SC. Moreover, the as-fabricated quasi-solid-state SC with the FNG electrode shows excellent cyclic stability, as evidenced by a satisfactory capacitance retention of 91.2% after 10000 cycles (Figure S27).

Conclusions. In summary, nitrogen-doped graphene has been prepared via an ultrafast FJH method for high-rate supercapacitors. This synthetic process helps the conversion of amorphous carbon to crystalline graphene and is free of solvents, catalysts, and gases. The resultant FNG flakes feature average layers of 2−6 together with high graphitization and a turbostratic structure. It exhibits desirable electrochemical energy storage performance in terms of large surface-area-normalized capacitance of 152.8 μF cm^{-2} at 1 A g^{-1}, facilitating both electron and ion transport (τ_0 = 30.2 ms), and a excellent rate capability as 86.1% capacitance can be maintained at an extremely high current density of 128 A g^{-1}. Additionally, the assembled symmetric quasi-solid-state SC with the FNG electrode affords a high energy density of 16.9 Wh kg^{-1} and capacitance retention of 91.2% after 10000 cycles, thus demonstrating the great potential of the FNG material in practical applications.

■ ASSOCIATED CONTENT

Supporting Information

The Supporting Information is available free of charge at https://pubs.acs.org/doi/10.1021/acsmaterialslett.2c00616.

Experimental details, materials characterization, and electrochemical results (PDF)

■ AUTHOR INFORMATION

Corresponding Authors

Sheng Zhu − *Institute of Molecular Science, Key Lab of Materials for Energy Conversion and Storage of Shanxi Province, Key Laboratory of Chemical Biology and Molecular Engineering of Education Ministry, Shanxi University, Taiyuan 030006, China;* orcid.org/0000-0003-1713-0621; Email: shengzhu@sxu.edu.cn

Si-Dian Li − *Institute of Molecular Science, Key Lab of Materials for Energy Conversion and Storage of Shanxi Province, Key Laboratory of Chemical Biology and Molecular Engineering of Education Ministry, Shanxi University, Taiyuan 030006, China;* orcid.org/0000-0001-5666-0591; Email: lisidian@sxu.edu.cn

Gaoyi Han − *Institute of Molecular Science, Key Lab of Materials for Energy Conversion and Storage of Shanxi Province, Key Laboratory of Chemical Biology and Molecular Engineering of Education Ministry, Shanxi University, Taiyuan 030006, China;* orcid.org/0000-0002-7019-3392; Email: han_gaoyis@sxu.edu.cn

Yan Li − *Beijing National Laboratory for Molecular Science, Key Laboratory for the Physics and Chemistry of Nanodevices, State Key Laboratory of Rare Earth Materials Chemistry and Applications, College of Chemistry and Molecular Engineering, Peking University, Beijing 100871, China;* orcid.org/0000-0002-3828-8340; Email: yanli@pku.edu.cn

Authors

Fei Zhang − *Institute of Molecular Science, Key Lab of Materials for Energy Conversion and Storage of Shanxi Province, Key Laboratory of Chemical Biology and Molecular Engineering of Education Ministry, Shanxi University, Taiyuan 030006, China*

Hai-Gang Lu − *Institute of Molecular Science, Key Lab of Materials for Energy Conversion and Storage of Shanxi Province, Key Laboratory of Chemical Biology and Molecular Engineering of Education Ministry, Shanxi University, Taiyuan 030006, China*

Jian Sheng − *Beijing National Laboratory for Molecular Science, Key Laboratory for the Physics and Chemistry of Nanodevices, State Key Laboratory of Rare Earth Materials Chemistry and Applications, College of Chemistry and Molecular Engineering, Peking University, Beijing 100871, China*

Lina Wang − *Institute of Molecular Science, Key Lab of Materials for Energy Conversion and Storage of Shanxi Province, Key Laboratory of Chemical Biology and Molecular Engineering of Education Ministry, Shanxi University, Taiyuan 030006, China*

Complete contact information is available at: https://pubs.acs.org/10.1021/acsmaterialslett.2c00616

Author Contributions

CRediT: **Sheng Zhu** data curation, funding acquisition, methodology, resources, writing-original draft; **Fei Zhang** data curation, methodology, validation; **Hai-Gang Lu** conceptualization, methodology, visualization; **Jian Sheng** investigation, methodology; **Lina Wang** investigation, methodology; **Si-Dian Li** funding acquisition, supervision, writing-review & editing; **Gaoyi Han** funding acquisition, supervision, validation, writing-review & editing; **Yan Li** funding acquisition, supervision, visualization, writing-review & editing.

Notes

The authors declare no competing financial interest.

■ ACKNOWLEDGMENTS

This work was supported by the Science and Technology Major Project of Shanxi (No. 202101030201022), the Fundamental Research Program of Shanxi Province (No. 202103021223019), and the National Natural Science Foundation of China (Grant Nos. 22120102004 and 21720102006).

■ REFERENCES

(1) Huang, P.; Lethien, C.; Pinaud, S.; Brousse, K.; Laloo, R.; Turq, V.; Respaud, M.; Demortiere, A.; Daffos, B.; Taberna, P. L.; Chaudret, B.; Gogotsi, Y.; Simon, P. On-chip and freestanding elastic carbon films for micro-supercapacitors. *Science* **2016**, *351*, 691−695.

(2) Salanne, M.; Rotenberg, B.; Naoi, K.; Kaneko, K.; Taberna, P.-L.; Grey, C. P.; Dunn, B.; Simon, P. Efficient storage mechanisms for building better supercapacitors. *Nat. Energy* **2016**, *1*, 1−10.

(3) Dubal, D. P.; Chodankar, N. R.; Kim, D.-H.; Gomez-Romero, P. Towards flexible solid-state supercapacitors for smart and wearable electronics. *Chem. Soc. Rev.* **2018**, *47*, 2065−2129.

(4) Chen, D.; Jiang, K.; Huang, T.; Shen, G. Recent advances in fiber supercapacitors: materials, device configurations, and applications. *Adv. Mater.* **2020**, *32*, 1901806.

(5) Wang, R.; Yao, M.; Niu, Z. Smart supercapacitors from materials to devices. *InfoMat* **2020**, *2*, 113−125.
(6) Xu, K.; Shao, H.; Lin, Z.; Merlet, C.; Feng, G.; Zhu, J.; Simon, P. Computational insights into charge storage mechanisms of supercapacitors. *Energy Environm. Mater.* **2020**, *3*, 235−246.
(7) Forse, A. C.; Merlet, C.; Griffin, J. M.; Grey, C. P. New perspectives on the charging mechanisms of supercapacitors. *J. Am. Chem. Soc.* **2016**, *138*, 5731−5744.
(8) Maiti, U. N.; Lim, J.; Lee, K. E.; Lee, W. J.; Kim, S. O. Three-dimensional shape engineered, interfacial gelation of reduced graphene oxide for high rate, large capacity supercapacitors. *Adv. Mater.* **2014**, *26*, 615−619.
(9) Shao, J.; Song, M.; Wu, G.; Zhou, Y.; Wan, J.; Ren, X.; Ma, F. 3D carbon nanocage networks with multiscale pores for high-rate supercapacitors by flower-like template and in-situ coating. *Energy Storage Mater.* **2018**, *13*, 57−65.
(10) El-Kady, M. F.; Shao, Y.; Kaner, R. B. Graphene for batteries, supercapacitors and beyond. *Nat. Rev. Mater.* **2016**, *1*, 1−14.
(11) Zhang, S.; Pan, N. Supercapacitors performance evaluation. *Adv. Energy Mater.* **2015**, *5*, 1401401.
(12) Kim, H.-S.; Cook, J. B.; Lin, H.; Ko, J. S.; Tolbert, S. H.; Ozolins, V.; Dunn, B. Oxygen vacancies enhance pseudocapacitive charge storage properties of MoO_{3-x}. *Nat. Mater.* **2017**, *16*, 454−460.
(13) Zhu, S.; Wang, Y.; Zhang, J.; Sheng, J.; Yang, F.; Wang, M.; Ni, J.; Jiang, H.; Li, Y. Jahn-Teller effect directed bandgap tuning of birnessite for pseudocapacitive application. *Energy Environ. Mater.* **2022**, DOI: 10.1002/eem2.12382.
(14) Javed, M. S.; Shaheen, N.; Hussain, S.; Li, J.; Shah, S. S. A.; Abbas, Y.; Ahmad, M. A.; Raza, R.; Mai, W. An ultra-high energy density flexible asymmetric supercapacitor based on hierarchical fabric decorated with 2D bimetallic oxide nanosheets and MOF-derived porous carbon polyhedra. *J. Mater. Chem. A* **2019**, *7*, 946−957.
(15) Raymundo-Piñero, E.; Cadek, M.; Béguin, F. Tuning carbon materials for supercapacitors by direct pyrolysis of seaweeds. *Adv. Funct. Mater.* **2009**, *19*, 1032−1039.
(16) Wang, Q.; Yan, J.; Fan, Z. Carbon materials for high volumetric performance supercapacitors: design, progress, challenges and opportunities. *Energy Environ. Sci.* **2016**, *9*, 729−762.
(17) Zhu, S.; Ni, J.; Li, Y. Carbon nanotube-based electrodes for flexible supercapacitors. *Nano Res.* **2020**, *13*, 1825−1841.
(18) Chee, W. K.; Lim, H. N.; Zainal, Z.; Huang, N. M.; Harrison, I.; Andou, Y. Flexible graphene-based supercapacitors: a review. *J. Phys. Chem. C* **2016**, *120*, 4153−4172.
(19) Yoo, J. J.; Balakrishnan, K.; Huang, J.; Meunier, V.; Sumpter, B. G.; Srivastava, A.; Conway, M.; Mohana Reddy, A. L.; Yu, J.; Vajtai, R.; Ajayan, P. M. Ultrathin planar graphene supercapacitors. *Nano Lett.* **2011**, *11*, 1423−1427.
(20) Li, X.; Zhi, L. Graphene hybridization for energy storage applications. *Chem. Soc. Rev.* **2018**, *47*, 3189−3216.
(21) Liu, L.; Yu, Y.; Yan, C.; Li, K.; Zheng, Z. Wearable energy-dense and power-dense supercapacitor yarns enabled by scalable graphene-metallic textile composite electrodes. *Nat. Commun.* **2015**, *6*, 7260.
(22) Xiong, Z.; Liao, C.; Han, W.; Wang, X. Mechanically tough large-area hierarchical porous graphene films for high-performance flexible supercapacitor applications. *Adv. Mater.* **2015**, *27*, 4469−4475.
(23) Xu, S.; Wen, Y.; Chen, Z.; Ji, N.; Zou, Z.; Wu, M.; Qu, L.; Zhang, J. Vertical graphene arrays as electrodes for ultra-high energy density AC line-filtering capacitors. *Angew. Chem., Int. Ed.* **2021**, *133*, 24710−24714.
(24) Pham, T. V.; Kim, J. G.; Jung, J. Y.; Kim, J. H.; Cho, H.; Seo, T. H.; Lee, H.; Kim, N. D.; Kim, M. J. High areal capacitance of N-doped graphene synthesized by arc discharge. *Adv. Funct. Mater.* **2019**, *29*, 1905511.
(25) Raccichini, R.; Varzi, A.; Passerini, S.; Scrosati, B. The role of graphene for electrochemical energy storage. *Nat. Mater.* **2015**, *14*, 271−279.
(26) Wang, B.; Ruan, T.; Chen, Y.; Jin, F.; Peng, L.; Zhou, Y.; Wang, D.; Dou, S. Graphene-based composites for electrochemical energy storage. *Energy Storage Mater.* **2020**, *24*, 22−51.
(27) Chen, J.; Yao, B.; Li, C.; Shi, G. An improved Hummers method for eco-friendly synthesis of graphene oxide. *Carbon* **2013**, *64*, 225−229.
(28) Huo, C.; Yan, Z.; Song, X.; Zeng, H. 2D materials via liquid exfoliation: a review on fabrication and applications. *Sci. Bull.* **2015**, *60*, 1994−2008.
(29) Weatherup, R. S.; Dlubak, B.; Hofmann, S. Kinetic control of catalytic CVD for high-quality graphene at low temperatures. *ACS Nano* **2012**, *6*, 9996−10003.
(30) Luan, Y.; Yin, J.; Zhu, K.; Cheng, K.; Yan, J.; Ye, K.; Wang, G.; Cao, D. Arc-discharge production of high-quality fluorine-modified graphene as anode for Li-ion battery. *Chem. Eng. J.* **2020**, *392*, 123668.
(31) Luong, D. X.; Bets, K. V.; Algozeeb, W. A.; Stanford, M. G.; Kittrell, C.; Chen, W.; Salvatierra, R. V.; Ren, M.; McHugh, E. A.; Advincula, P. A.; Wang, Z.; Bhatt, M.; Guo, H.; Mancevski, V.; Shahsavari, R.; Yakobson, B. I.; Tour, J. M. Gram-scale bottom-up flash graphene synthesis. *Nature* **2020**, *577*, 647−651.
(32) Stanford, M. G.; Bets, K. V.; Luong, D. X.; Advincula, P. A.; Chen, W.; Li, J. T.; Wang, Z.; McHugh, E. A.; Algozeeb, W. A.; Yakobson, B. I.; Tour, J. M. Flash graphene morphologies. *ACS Nano* **2020**, *14*, 13691−13699.
(33) Barbhuiya, N. H.; Kumar, A.; Singh, A.; Chandel, M. K.; Arnusch, C. J.; Tour, J. M.; Singh, S. The future of flash graphene for the sustainable management of solid waste. *ACS Nano* **2021**, *15*, 15461−15470.
(34) Li, Z.; Lu, C.; Xia, Z.; Zhou, Y.; Luo, Z. X-ray diffraction patterns of graphite and turbostratic carbon. *Carbon* **2007**, *45*, 1686−1695.
(35) Chen, W.; Ge, C.; Li, J. T.; Beckham, J. L.; Yuan, Z.; Wyss, K. M.; Advincula, P. A.; Eddy, L.; Kittrell, C.; Chen, J.; Luong, D. X.; Carter, R. A.; Tour, J. M. Heteroatom-doped flash graphene. *ACS Nano* **2022**, *16*, 6646−6656.
(36) Indrawirawan, S.; Sun, H.; Duan, X.; Wang, S. Low temperature combustion synthesis of nitrogen-doped graphene for metal-free catalytic oxidation. *J. Mater. Chem. A* **2015**, *3*, 3432−3440.
(37) Malard, L.; Pimenta, M. A.; Dresselhaus, G.; Dresselhaus, M. Raman spectroscopy in graphene. *Phys. Rep.* **2009**, *473*, 51−87.
(38) Ferrari, A. C.; Basko, D. M. Raman spectroscopy as a versatile tool for studying the properties of graphene. *Nat. Nanotechnol.* **2013**, *8*, 235−246.
(39) Eckmann, A.; Felten, A.; Mishchenko, A.; Britnell, L.; Krupke, R.; Novoselov, K. S.; Casiraghi, C. Probing the nature of defects in graphene by Raman spectroscopy. *Nano Lett.* **2012**, *12*, 3925−3930.
(40) Gao, J.; Wang, Y.; Wu, H.; Liu, X.; Wang, L.; Yu, Q.; Li, A.; Wang, H.; Song, C.; Gao, Z.; Peng, M.; Zhang, M.; Ma, N.; Wang, J.; Zhou, W.; Wang, G.; Yin, Z.; Ma, D. Construction of a sp^3/sp^2 carbon interface in 3D N-doped nanocarbons for the oxygen reduction reaction. *Angew. Chem., Int. Ed.* **2019**, *131*, 15233−15241.
(41) Díaz, J.; Paolicelli, G.; Ferrer, S.; Comin, F. Separation of the sp^3 and sp^2 components in the C1s photoemission spectra of amorphous carbon films. *Phys. Rev. B* **1996**, *54*, 8064.
(42) Athanasiou, M.; Samartzis, N.; Sygellou, L.; Dracopoulos, V.; Ioannides, T.; Yannopoulos, S. N. High-quality laser-assisted biomass-based turbostratic graphene for high-performance supercapacitors. *Carbon* **2021**, *172*, 750−761.
(43) Zhu, S.; Wang, L.; Gu, C.; Liu, H.; Mu, Y.; Ni, J.; Han, G. Boosting capacitive performance of nitrogen-doped carbon by atomically dispersed iron. *J. Power Sources* **2022**, *532*, 231335.
(44) Javed, M. S.; Shah, S. S. A.; Najam, T.; Siyal, S. H.; Hussain, S.; Saleem, M.; Zhao, Z.; Mai, W. Achieving high-energy density and superior cyclic stability in flexible and lightweight pseudocapacitor through synergic effects of binder-free $CoGa_2O_4$ 2D-hexagonal nanoplates. *Nano Energy* **2020**, *77*, 105276.
(45) Javed, M. S.; Shah, S. S. A.; Hussain, S.; Tan, S.; Mai, W. Mesoporous manganese-selenide microflowers with enhanced electro-

chemical performance as a flexible symmetric 1.8 V supercapacitor. *Chem. Eng. J.* **2020**, *382*, 122814.
(46) Lin, S.; Tang, J.; Zhang, K.; Suzuki, T. S.; Wei, Q.; Mukaida, M.; Zhang, Y.; Mamiya, H.; Yu, X.; Qin, L.-C. High-rate supercapacitor using magnetically aligned graphene. *J. Power Sources* **2021**, *482*, 228995.
(47) Chi, F.; Hu, Y.; He, W.; Weng, C.; Cheng, H.; Li, C.; Qu, L. Graphene ionogel ultra-fast filter supercapacitor with 4 V workable window and 150 °C operable temperature. *Small* **2022**, *18*, 2200916.
(48) Yang, C.; Schellhammer, K. S.; Ortmann, F.; Sun, S.; Dong, R.; Karakus, M.; Mics, Z.; Löffler, M.; Zhang, F.; Zhuang, X.; Cánovas, E.; Cuniberti, G.; Bonn, M.; Feng, X. Coordination polymer framework based on-chip micro-supercapacitors with AC line-filtering performance. *Angew. Chem., Int. Ed.* **2017**, *56*, 3920−3924.
(49) Zhang, S.; Pan, N. Supercapacitors performance evaluation. *Adv. Energy Mater.* **2015**, *5*, 1401401.
(50) Shao, Y.; Li, J.; Li, Y.; Wang, H.; Zhang, Q.; Kaner, R. B. Flexible quasi-solid-state planar micro-supercapacitor based on cellular graphene films. *Mater. Horiz.* **2017**, *4*, 1145−1150.

https://doi.org/10.1021/acsmaterialslett.2c00616
ACS Materials Lett. 2022, 4, 1863−1871